

Performance improvement of MF-DFA on feature extraction of skin lesion images

Jian Wang^{*,†,‡,||,††}, Yudong Zhang^{*}, Zhaohu Wang[§], Wenjing Jiang^{*},
Mengdie Yang^{*}, Menghao Huang^{*} and Junseok Kim^{¶,**,††}

**School of Mathematics and Statistics,
Nanjing University of Information Science and Technology,
Nanjing 210044, China*

*†Center for Applied Mathematics of Jiangsu Province,
Nanjing University of Information Science and Technology,
Nanjing 210044, China*

*‡Jiangsu International Joint Laboratory on System
Modeling and Data Analysis,
Nanjing University of Information Science and Technology,
Nanjing 210044, China*

*§School of Marketing and Logistics Management,
Nanjing University of Finance and Economics,
Nanjing 210023, China*

*¶Department of Mathematics, Korea University,
Seoul 02841, Republic of Korea*

||003328@nuist.edu.cn

***cfdkim@korea.ac.kr*

Received 14 February 2022

Revised 4 October 2022

Accepted 8 November 2022

Published 18 January 2023

In this paper, we propose an improved algorithm based on the original two-dimensional (2D) multifractal detrended fluctuation analysis (2D MF-DFA) that involves increasing the number of cumulative summations in the computational steps of 2D MF-DFA. The proposed method aims to modify the distribution of the generalized Hurst exponent to ensure that skin lesion image features are extracted based on enhanced multifractal features. We calculate the generalized Hurst exponent using 0, 1, or 2 cumulative summation processes. A support vector machine (SVM) is adopted to examine the classification

^{††}Corresponding authors.

performance under these three conditions. Computation shows that the process involving two cumulative summations achieves an accuracy, sensitivity, and specificity of $95.69 \pm 0.1174\%$, $94.25 \pm 0.0942\%$, and $97.63 \pm 0.1466\%$, respectively, which indicates that its performance is much better than with 0 and 1 cumulative summations.

Keywords: MF-DFA; cumulative summation; hurst exponent; SVM.

1. Introduction

Fractals and multifractals have many peculiar properties, which are worth studying.^{1–5} Multifractal detrended fluctuation analysis (MF-DFA) has been proposed for investigating complex nonlinear systems.⁶ Over the years, extensions to the basic method have greatly enhanced its applicability of MF-DFA. MF-DFA has so far been widely applied to many research fields. For instance, Aslam *et al.*⁷ used it to investigate the multifractal behavior of frontier markets and the long-term dependence of emerging Asian stock markets. Milos *et al.*⁸ used it to investigate the stock market indexes of seven Central and Eastern European countries. Tang *et al.*⁹ developed a fault-diagnosis method for nonlinear analog circuits based on MF-DFA. MF-DFA has also been used to study the nonlinear time-series analysis of friction brake vibration data,¹⁰ to detect and classify AC and DC side faults,¹¹ and to perform multifractal analysis of daily rainfall time series in the Pearl River basin.¹² Pavlov *et al.*¹³ used MF-DFA to consider the cerebrovascular response to sudden changes in peripheral arterial pressure in rats.

MF-DFA has many additional applications in feature extraction. For instance, aiming at various fault locations and damage degrees of rolling bearing signals, Xiong *et al.*¹⁴ developed a novel fault diagnosis algorithm using MF-DFA to extract features and intelligently classify various fault locations and damage degrees. Ruzbeshi *et al.*¹⁵ used attention deficit hyperactivity disorder as an example, and proposed two different feature extraction methods from the MF-DFA of EEG signals in Ref. 16. MF-DFA is used to extract the characteristic parameters of the GIS partial discharge signals. The results confirmed that the feature extraction method can effectively identify four types of insulation defects, even in the presence of strong background noise. Li *et al.*¹⁷ extracted friction vibration characteristics through technology and friction state recognition. Using the generalized Hurst exponent, the scaling exponent, and a multifractal spectrum, Lin *et al.*¹⁸ quantified the multifractality of bearing failure data. For more applications of MF-DFA in feature extraction, we refer the reader to Refs. 19–23 and references therein. Furthermore, as an important extension, Gu *et al.*²⁴ applied 2D MF-DFA to investigate multifractal surfaces. Wang *et al.*²⁵ applied the 2D multiscale multifractal analysis (MMA) method to investigate the multifractal properties of a 2D surface at multiple scales. Although MF-DFA is widely used in image feature extraction and classification, there remains significant scope for improvement. The automatic diagnosis of skin lesion images has been an important tool for clinical auxiliary diagnosis.²⁶ Hence, in this study, we optimize the internal structure of MF-DFA to improve the feature extraction and classification performance of the traditional model applied to

skin lesion images. The generalized Hurst exponent, extracted from the improved model, was used as the digital attribute for benign and malignant lesions. Taken as an input feature of a support vector machine (SVM), it can be used for skin lesion image recognition. Various classification studies on skin lesion images have also been conducted.²⁷ In this study, we apply 2D MF-DFA to two-dimensional skin lesion images to explore whether the SVM classification performance can be improved after different accumulations.

This paper is arranged as follows. Section 2 describes the method. Section 3 presents the data used in this study. We then present the numerical experiments in Sec. 4. Section 5 concludes.

2. Methodology

2.1. 2D MF-DFA

The 2D MF-DFA method has been widely used for feature extraction. Here, we briefly introduce a 2D MF-DFA algorithm.²⁴ Because the following numerical simulation is mainly based on images 128×128 and 256×256 , the image in the method description can be regarded as a square. A given 2D image is discretized into an $A \times B$ matrix $X = X_{i,j}$, where $A = B$. The surface is partitioned into $A_s \times B_s$ disjoint square segments of the same size $s \times s$, where A_s is $[A/s]$ and B_s is $[B/s]$. Specifically, A_s and B_s are positive intervals. The subarea is defined by $X_{a,b}(i_1, i_2) = X((a-1)s + i_1, (b-1)s + i_2)$. Subsequently, the cumulative summation $\Phi_{a,b}$ of the surface pixels for each subarea is calculated as

$$\Phi_{a,b}(i_1, i_2) = \sum_{j_1=1}^{i_1} \sum_{j_2=1}^{i_2} X_{a,b}(j_1, j_2), \quad (1)$$

where $1 \leq i_1, i_2 \leq s$, $a = 1, 2, \dots, A_s$ and $b = 1, 2, \dots, B_s$.

Second, the trend of the constructed surface $\Phi_{a,b}(i_1, i_2)$ can be determined by fitting it with a prechosen bivariate polynomial function $\bar{\Phi}_{a,b}(i_1, i_2)$. The simplest function is a plane. In this study, we obtain the fitting polynomial using the function $\bar{\Phi}_{a,b}(i_1, i_2) = \alpha_1 i_1 + \alpha_2 i_2 + \beta$, where α_1 , α_2 , and β are undetermined free parameters that can be calculated using the least squares method. The residual $\phi_{a,b}(i_1, i_2)$ is defined as

$$\phi_{a,b}(i_1, i_2) = \Phi_{a,b}(i_1, i_2) - \bar{\Phi}_{a,b}(i_1, i_2). \quad (2)$$

Subsequently, based on the residual matrix, the detrended fluctuation function $F^2(a, b, s)$ of each subarea is calculated using the following equation:

$$F^2(a, b, s) = \frac{1}{s^2} \sum_{i_1=1}^s \sum_{i_2=1}^s (\phi_{a,b}(i_1, i_2))^2. \quad (3)$$

Next, we calculate the q th-order fluctuation function of all the subareas according to the detrended fluctuation function of each subarea:

$$F_q(s) = \begin{cases} \left\{ \frac{1}{A_s B_s} \sum_{a=1}^{A_s} \sum_{b=1}^{B_s} [F(a, b, s)]^q \right\}^{\frac{1}{q}} & \text{if } q \neq 0, \\ \exp \left(\frac{1}{A_s A_s} \sum_{a=1}^{A_s} \sum_{b=1}^{B_s} \ln [F(a, b, s)] \right) & \text{if } q = 0. \end{cases} \quad (4)$$

When s increases, $F_q(s)$ increases according to the power relationship:

$$F_q(s) \propto s^{h(q)}, \quad (5)$$

where $h(q)$ is the generalized Hurst exponent that represents the image features.

The following scaling exponent $\tau(q)$ is also an important index to measure the multifractal characteristics, where D_f is the fractal dimension supported by the multifractal measure geometry.⁶

$$\tau(q) = qh(q) - D_f. \quad (6)$$

2.2. Cumulative summation

A regular sequence does not require the cumulative summation. The “regular sequence” here refers to a sequence with a small trend fluctuation, whose characteristic values can be extracted without a cumulative summation. Continued cumulative summation increases the generalized Hurst exponent. In the context of feature extraction, a large Hurst exponent implies large feature values. Therefore, a wider characteristic interval yields more obvious feature values a greater classification accuracy. When a given sequence cannot show a relatively regular trend, cumulative summation enhances steadiness. However, increasing the cumulative summation times has drawbacks because it may result in over-fitting problem during feature extraction. The intuitive manifestation of over-fitting is that the algorithm performs well on a training set but fails in its generalization when applied to a test set. In this study, the function of the first cumulative summation is given as follows:

$$\Phi_{a,b}(i_1, i_2) = \sum_{j_1=1}^{i_1} \sum_{j_2=1}^{i_2} X_{a,b}(j_1, j_2). \quad (7)$$

The equation of quadratic cumulative summation is

$$\widetilde{\Phi}_{a,b}(i_1, i_2) = \sum_{j_1=1}^{i_1} \sum_{j_2=1}^{i_2} (\Phi_{a,b}(j_1, j_2)). \quad (8)$$

Figure 1 shows schematically the overall procedure of the proposed classification algorithm.

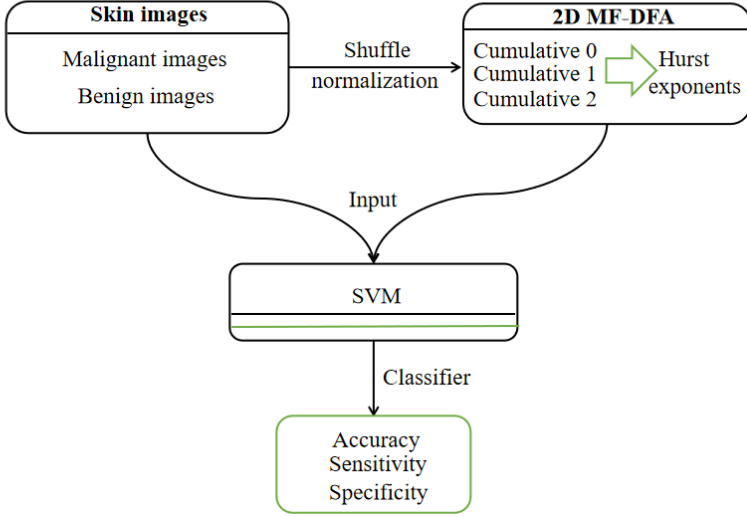


Fig. 1. Procedure of the proposed algorithm.

2.3. Multiplicative cascade image

Now, we synthesize multiplicative cascades to examine the performance of cumulative summation. The classical multiplicative cascade method in theoretical physics can produce rich multifractal structures with rich deterministic or uncertain properties.^{28–31} In this paper, we use p -model to synthesize two-dimensional multifractal images. First, the area of a large square image is determined, and then divide evenly into four small square images. After that, each sub-image continues to be divided equally into four smaller square images. This process is repeated n times to get the final generated multiplicative cascade image. Among them, image pixels are determined by four parameters P_1, P_2, P_3 and P_4 , and $P_1 + P_2 + P_3 + P_4 = 1$. The size of B determines the black proportion of the generated multiplicative cascade image. To achieve the best visual effect, set $B = 10^5$.

We set $P_1 = 0.05, P_2 = 0.15, P_3 = 0.3, P_4 = 0.5$ and $N = 8$. The resulting multiplicative cascade image is shown in Fig. 2 (a). Furthermore, we add outliers to a small part of the inside of the image to get the abnormal image, as shown in Fig. 2(b).

Before numerical simulation, we first apply 1 and 2-times cumulative summation to the original multiplicative cascaded image and the abnormal multiplicative cascaded image to extract multifractal features, respectively. The parameter q of 2D MF-DFA is set to vary between -15 and 15 , and the variation is divided into 11 segments. Parameter s is set to vary stably between 15 and 30. Figure 3 shows that both h_q and τ_q are much more sensitive to outliers than the 1-time cumulative summation.

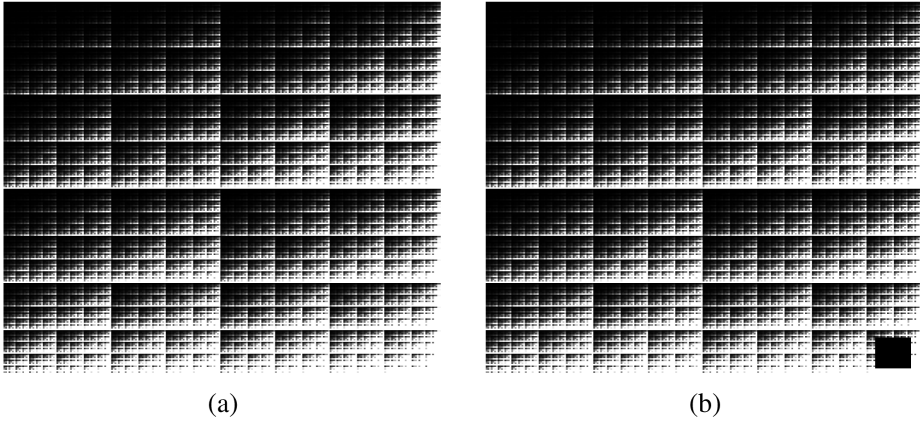


Fig. 2. Multiplicative cascade images (a) original image, (b) abnormal image.

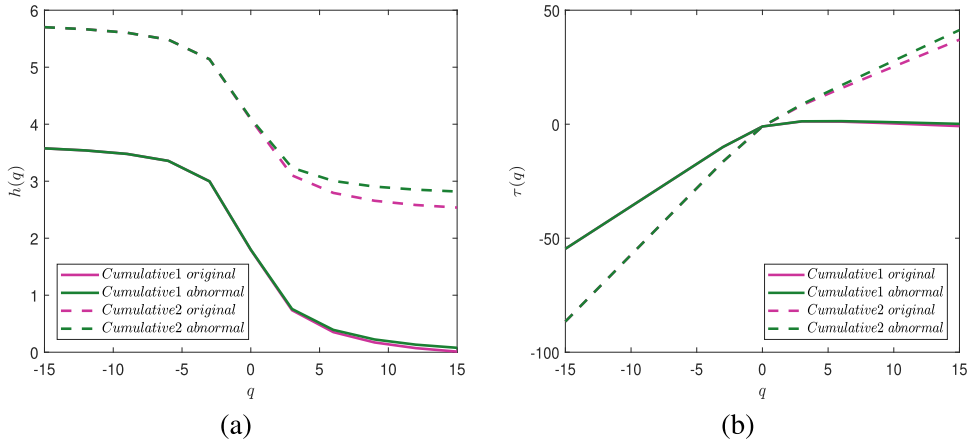


Fig. 3. Local generalized Hurst exponent h_q and τ_q obtained using optimized 2D MF-DFA with (a) 1 and (b) 2 accumulations.

3. Data Collection

Sample data containing images of both benign and malignant skin lesions are downloaded from the “Isic Archive” for analysis. The size of the skin lesion images in this archive is 23 K. Each sample includes an image of the lesion and metadata relating to the patient. We randomly selected 36 images of nevus skin lesions and 36 images of melanoma, and normalize each image to 128×128 and 256×256 , respectively, to verify the effectiveness of the proposed algorithm. Computations in this study are processed using MATLAB R2020a software on an Intel(R) Core(TM) i5-4430 CPU @ 3.00 GHz processor.

4. Empirical Results

We conduct several numerical tests to demonstrate the robustness of the proposed algorithm. The data consisted of 36 images of skin nevus lesions and 36 images of melanoma with dimensions 128×128 . We validate the effectiveness of traditional 2D MF-DFA in the feature extraction of skin lesions. Then, we verify the accuracy of the multifractal theory in skin lesion image feature extraction using the proposed method. The main difference between this method and the traditional 2D MF-DFA method is that the constructed cumulative summation is accumulated successively 0 to 2 times. Furthermore, we use the SVM to incorporate the generalized Hurst exponent calculated by MF-DFA under different accumulative conditions into the classifier and analyze the classification performance of the optimized MF-DFA. The data set contains 72 skin lesion images, including 36 benign and 36 malignant skin-lesion images, without elaboration.

Using the above methods, we analyzed the multifractal features and generalized Hurst exponents of the benign and malignant skin lesions. The relevant parameters used for calculating the local generalized Hurst exponent are the segmentation scale s and fractal order q . According to Ref. 25, the minimum value of the segmented scale s is greater than the polynomial order, and the maximum is less than $1/6$ of the sample size. In this example, we let the minimum segment size to $s_{\min} = 2$ and the maximum to $s_{\max} = 9$. The value of q ranges from -30 to 30 in increments of 12 , i.e. the Hurst exponent took the values $-30, -18, -6, 6, 18$ and 30 .

We use traditional 2D MF-DFA to effectively extract the features of each image in the two categories and then compute the relationship between the local generalized Hurst exponent h_q and q . All these features are shown in Fig. 4.

We also apply the simplified and optimized 2D MF-DFA to extract the features of benign and malignant skin lesions, respectively. The generalized Hurst exponent distributions of the 0 and 2-times cumulative summation are shown in Figs. 5(a)

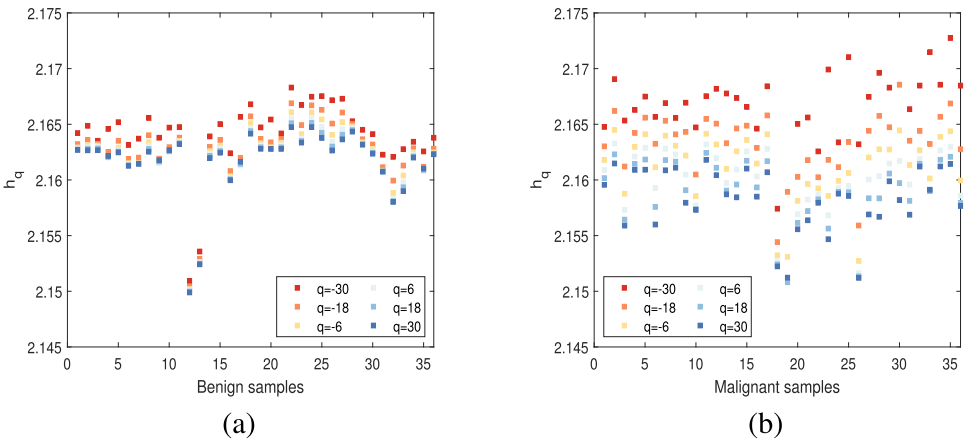


Fig. 4. Local generalized Hurst exponent h_q for (a) benign and (b) malignant skin lesion images.

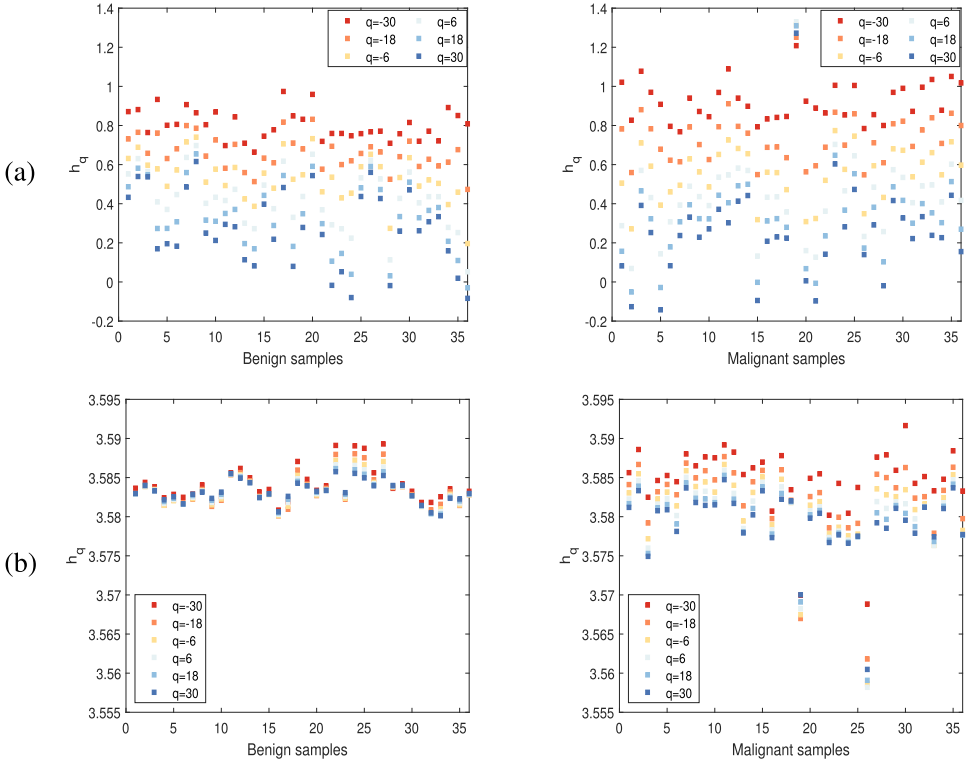


Fig. 5. (Color online) Local generalized Hurst exponent h_q obtained using optimized 2D MF-DFA with (a) 0 and (b) 2 accumulations.

and 5(b), respectively. Using the image surface accumulation in Eq. (9) starting from 0 to 2, we observe that Δh for both benign and malignant skin-lesion samples increase gradually, and the sample distribution is more concentrated. The feature distribution calculated by 2-times cumulative summation of two times for the benign and malignant images is clearly more distinguishable. We conclude that compared with traditional 2D MF-DFA, the proposed method may be more effective for extracting features. However, as mentioned above, using three or more cumulative summations results in an over-fitting of the image information extraction.

The distribution of the extracted feature values h_q in benign skin-lesion samples is clearly more focused than in the malignant lesion samples, based on Figs. 4 and 5. However, because the distinction of the generalized Hurst exponents is not obvious, we select three h_q of benign and malignant lesion samples to construct a three-dimensional image for observation and comparison. Figure 6 clearly shows that with the increment of the times of the cumulative summation, the overlapping part of the extracted features of the benign and malignant samples gradually decreases. The following 3D figure is only the spatial distribution of benign and malignant samples, which can be regarded as the input data of SVM. The specific

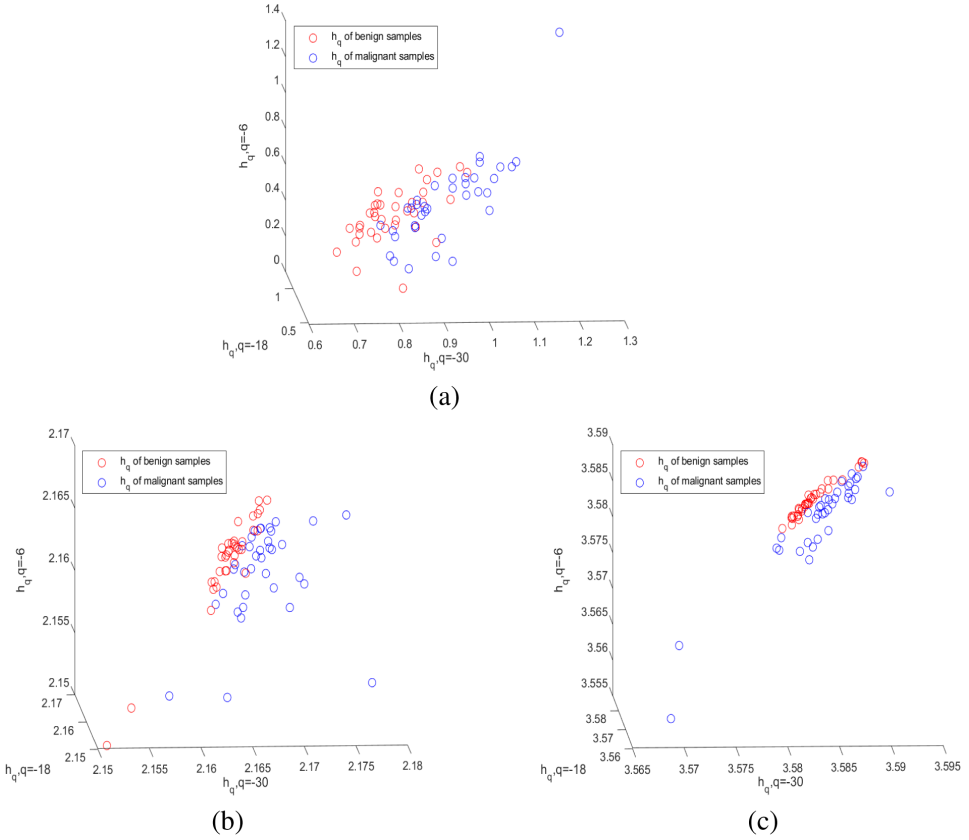


Fig. 6. (Color online) 128×128 images' distribution of h_q when q equals -6 , -18 and -30 for a cumulative summation count of (a) 0, (b) 1, and (c) 2, respectively.

classification process and accuracy should refer to the results of SVM binary classification.³² SVM is solved by establishing a quadratic programming primal problem, introducing Lagrange multiplier method, and then transforming it into a dual form to minimize the loss function. In fact, most of the time, the data is not linearly separable. As shown in Fig. 6, it is difficult to find the optimal hyperplane to classify benign and malignant lesion samples even if we perform quadratic accumulation. For the nonlinear case, the SVM processing method solves the problem of linear inseparability in the original space by mapping the data to a higher dimensional space through the kernel technique.

In the classification stage, we use the digital attributes of the two types of images extracted. In other words, the generalized Hurst exponent is used as the input of the SVM to search for the best hyperplane and classify melanoma and non-melanoma images. That is to say, the extracted h_q is only a step in our classification, and its change will have a great impact on the classification performance of SVM. Our classification performance depends on whether we can find the optimal hyperplane to

separate images of benign and malignant lesions, rather than the distance between the hurst exponent. The Accuracy, Sensitivity and Specificity are used to measure the performance of the proposed model and are calculated as follows:

$$\text{Accuracy} = \frac{\text{TP} + \text{TN}}{\text{TP} + \text{FN} + \text{FP} + \text{TN}}, \tag{9}$$

$$\text{Sensitivity} = \frac{\text{TP}}{\text{TP} + \text{FN}}, \tag{10}$$

$$\text{Specificity} = \frac{\text{TN}}{\text{FP} + \text{TN}}, \tag{11}$$

where TP (True Positive), FN (False Negative), TN (True Negative), and FP (False Positive), respectively, denote malignant being tagged as malignant, benign as malignant, benign as benign, and malignant as benign. Accuracy is used to represent the probability of correct sample recognition by the SVM and the sensitivity was used as the recognition rate of the model images. The specificity is used to detect melanoma. Owing to the small sample size of skin lesion image data, to use

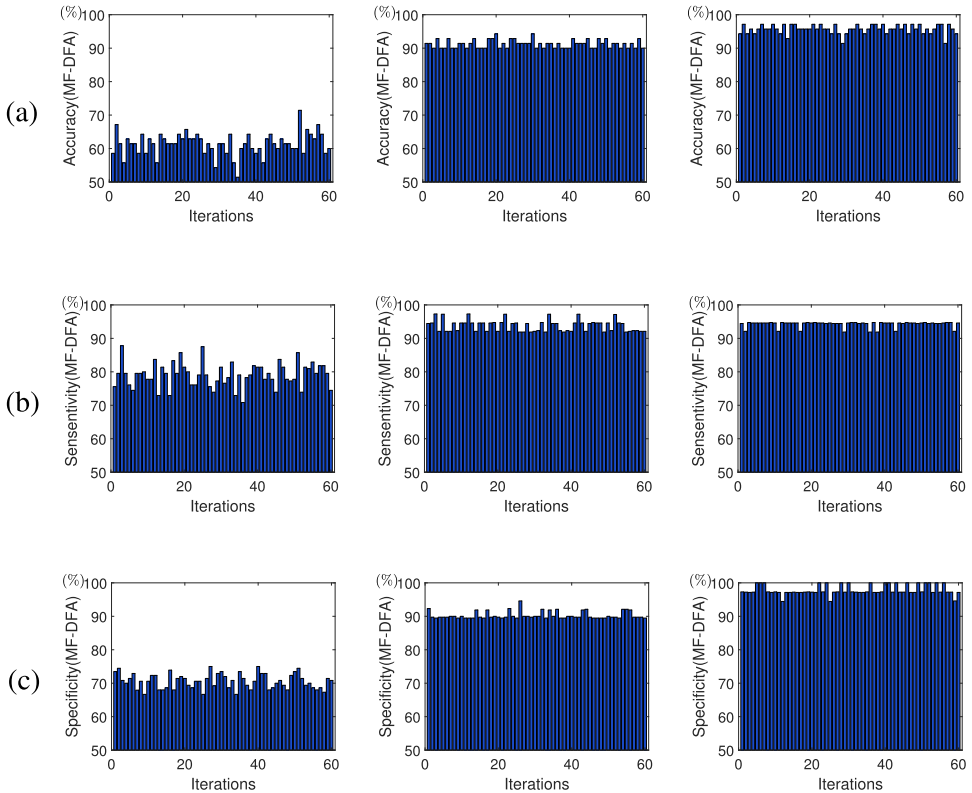


Fig. 7. (Color online) Evaluation indicators for the 128×128 image classification: (a) Accuracy, (b) Sensitivity, (c) Specificity. The columns, from left to right, refer to 0, 1, and 2 accumulations.

fewer test data to increase the accuracy of reliability, we can use the k-fold cross-validation method to conduct classification tests on the SVM. The two types of image samples were mixed for multiple scrambling, and the corresponding frequency group evaluation indexes were calculated. The means and standard deviation of the three evaluation indexes were used to quantify the final classification performance. The classification samples were randomly scrambled 60 times.

Figures 7(a)–7(c) show the SVM performance evaluation results for the Accuracy, Sensitivity and Specificity, respectively. The first column involves no cumulative summation (cumulative 0); the second column constructs the sum sequence of

Table 1. Classification of the classification performance of 128×128 images for the cases of 0, 1 and 2 cumulative sums.

Method	Accuracy	Sensitivity	Specificity
MF-DFA-SVM-cumulative 0	$61.36 \pm 0.1828\%$	$79.09 \pm 0.1903\%$	$70.59 \pm 0.1497\%$
MF-DFA-SVM-cumulative 1	$91.24 \pm 0.1104\%$	$93.77 \pm 0.1316\%$	$90.26 \pm 0.1056\%$
MF-DFA-SVM-cumulative 2	$95.69 \pm 0.1174\%$	$94.25 \pm 0.0942\%$	$97.63 \pm 0.1466\%$

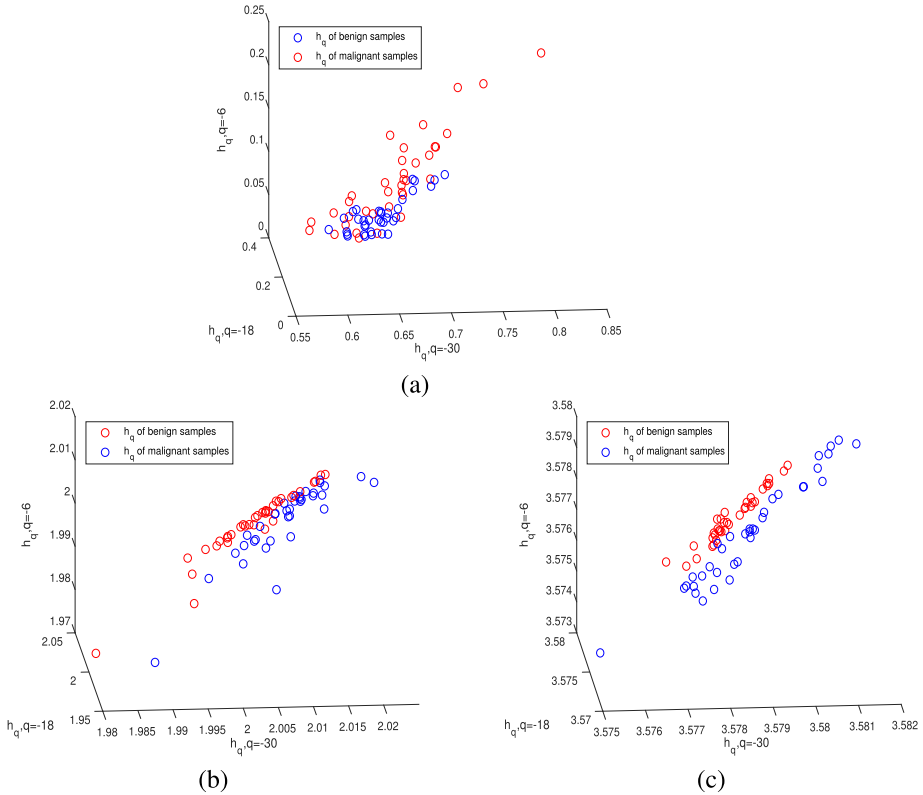


Fig. 8. (Color online) 256×256 images' distribution of h_q when q equals -6 , -18 and -30 for a cumulative summation count of (a) 0, (b) 1, and (c) 2, respectively.

the mean removal once (cumulative 1); and the third column constructs the cumulative summation twice (cumulative 2). Clearly, the three indicators in column 2 are much higher than those in column 1, and those in column 3 are higher than those in column 2. Thus, the best performing model is obtained after image surface construction of two cumulative summations. We conclude that different cumulative summation times are important for image feature extraction ability. Future work will investigate the most suitable number of cumulative summations to improve the algorithm performance.

To make the calculation results more intuitive, we calculated the mean value and standard deviation of the histogram, as shown in Fig. 7 and summarized in Table 1. The computational results show that the traditional MF-DFA model performs well in the feature extraction and classification of skin lesions. The Accuracy, Sensitivity and Specificity reached $91.24 \pm 0.1104\%$, $93.77 \pm 0.1316\%$ and $90.26 \pm 0.1056\%$, respectively. Nevertheless, the time required to construct a cumulative summation in the model significantly influences feature extraction and the classification performance. The model performance is significantly reduced when

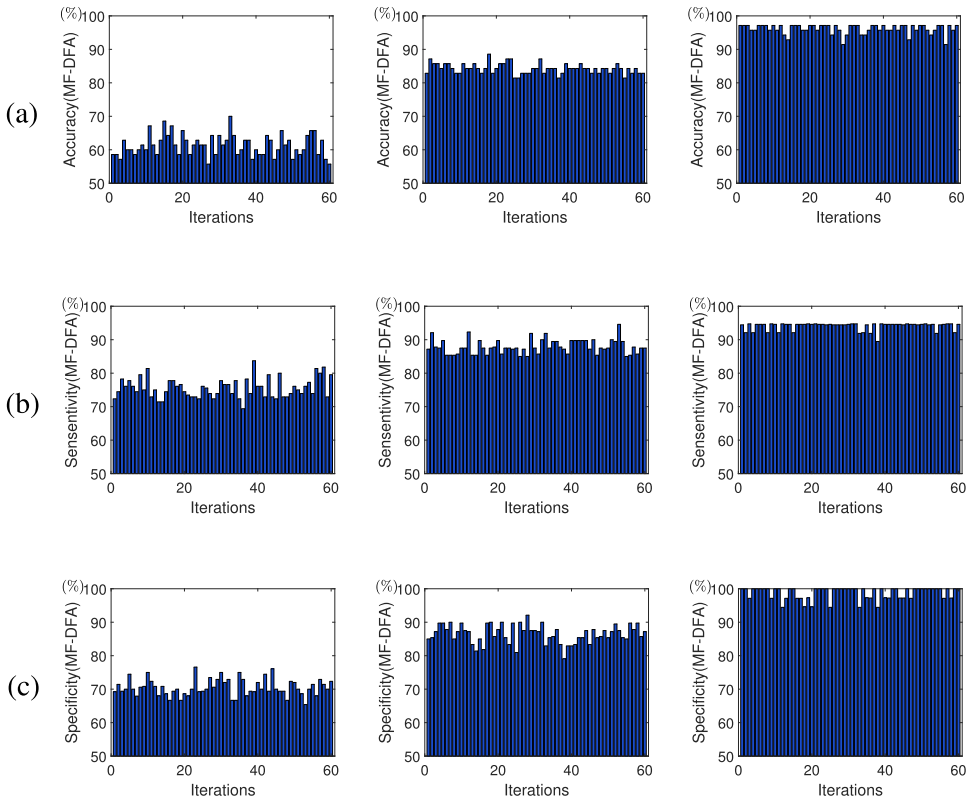


Fig. 9. (Color online) Evaluation indicators for the 256×256 image classification: (a) Accuracy, (b) Sensitivity, and (c) Specificity. Columns from left to right represent 0, 1, and 2 accumulations.

Table 2. Classification performance of 256×256 images compared for 0, 1, and 2 cumulative summations.

Method	Accuracy	Sensitivity	Specificity
MF-DFA-SVM-cumulative 0	$61.36 \pm 0.1790\%$	$75.58 \pm 0.1721\%$	$70.51 \pm 0.1583\%$
MF-DFA-SVM-cumulative 1	$82.24 \pm 0.1238\%$	$87.91 \pm 0.1463\%$	$86.53 \pm 0.1506\%$
MF-DFA-SVM-cumulative 2	$96.12 \pm 0.1201\%$	$94.09 \pm 0.1067\%$	$98.75 \pm 0.1366\%$

the cumulative sequence is not used, giving Accuracy, Sensitivity, and Specificity values of only $61.36 \pm 0.1828\%$, $79.09 \pm 0.1903\%$, and $70.59 \pm 0.1497\%$. Using the cumulative summation twice improves the model performance significantly, with the Accuracy, Sensitivity, and Specificity reaching $95.69 \pm 0.1174\%$, $94.25 \pm 0.0942\%$, and $97.63 \pm 0.1466\%$, respectively.

Finally, the effectiveness of the proposed method is verified. For this purpose, we adopt 36 skin nevus lesions and 36 melanoma images with size 256×256 . As above, we select three h_q of benign and malignant lesion samples to construct a three-dimensional image as shown in Fig. 8. Figures 9(a)–9(c) show the SVM performance evaluation results for the melanoma images in terms of the accuracy, sensitivity, and specificity, respectively. The first column involves no cumulative sum (cumulative 0); the second column constructs the summation sequence with one average removal (cumulative 1); and the third column constructs the cumulative summation (cumulative 2). The same conclusion can thus be drawn for images of size 256×256 , increasing the number of cumulative summations to two achieves the best classification performance. The corresponding means and standard deviations are also listed in Table 2.

5. Conclusions

Based on the traditional 2D MF-DFA method, we proposed an improved method to accumulate the summation step from 0 to 2. The proposed algorithm greatly improves the performance of skin cancer melanoma classification. We observed that the generalized Hurst exponent of 36 benign melanoma images and 36 malignant melanoma images, extracted using traditional 2D MF-DFA, can fully characterize the multifractal features of the target image. In addition, we conclude that the distribution of the generalized Hurst exponent extracted by the proposed improved algorithm can be changed by varying the number of cumulative summations. The multifractal feature distribution of the obtained target features was also gradually concentrated with an increase in cumulative summation times.

We performed zero, one, and two cumulative summation, and the calculated generalized Hurst exponent was used as the SVM input vector. Using the accuracy, sensitivity, and specificity as SVM classification indicators, we measured the impact of changing the cumulative number of steps in the traditional 2D MF-DFA method on the classification performance. The results showed that, as this number increases, all three classification indicators increased significantly. Among them,

the classification performance corresponding to zero cumulative summation was the worst, whereas the two cumulative summations achieved the best classification performance. We conclude that the improved method significantly increased the classification performance compared to traditional 2D MF-DFA. Future work will explore the applicability of this algorithm to other fields of medicine and beyond.

Acknowledgments

The first author Jian Wang would like to thank the Natural Science Foundation of the Jiangsu Higher Education Institutions of China (Grant No. 22KJB110020). The corresponding author (J. S. Kim) was supported by the Korea University Grant. The authors would like to thank the reviewers for their constructive and helpful comments for the revision of this paper.

References

1. S. A. Nejad, T. Stosic and B. Stosic, *Fractals* **29** (2021) 2150010.
2. A. Bershanskii, *Mod. Phys. Lett. B* **12** (1998) 11.
3. V. V. Mitic, C. Fleshman, J. G. Duh, I. D. Ilic and G. Lazovic, *Mod. Phys. Lett. B* **35** (2021) 2150427.
4. C. Zeng, Y. Huang and Y. Xue, *Mod. Phys. Lett. B* **36** (2022) 2250109.
5. N. J. Francois, M. P. Losada and M. E. Daraio, *Fractals* **19** (2011) 339.
6. J. W. Kantelhardt, S. A. Zschiegner, E. Koscielny-Bunde, S. Havlin, A. Bunde and H. E. Stanley, *Physica A* **316** (2002) 87.
7. F. Aslam, S. Latif and P. Ferreira, *Symmetry* **12** (2020) 1157.
8. L. R. Milos, C. Hatiegan, M. C. Milos, F. M. Barna and C. Botoc, *Sustainability* **12** (2020) 535.
9. J. Y. Tang, J. M. Chen and C. Zhang, *Appl. Mech. Mater.* **263** (2013) 108.
10. N. K. Vitanov, N. P. Hoffmann and B. Wernitz, *Chaos Solitons Fractals* **69** (2014) 90.
11. E. N. Prasad and P. K. Dash, *Int. Trans. Electr. Energy Syst.* **31** (2021) e12564.
12. Z. G. Yu, Y. Leung, Y. D. Chen, Q. Zhang, V. Anh and Y. Zhou, *Physica A* **405** (2014) 193.
13. A. N. Pavlov, A. S. Abdurashitov, A. A. Koronovskii Jr, O. N. Pavlova, O. V. Semyachkina-Glushkovskaya and J. Kurths, *Commun. Nonlinear Sci.* **85** (2020) 105232.
14. Q. Xiong, W. Zhang, T. Lu, G. Mei and S. Liang, *Shock Vib.* **2016** (2016) 1232893.1.
15. Z. Roozbehi, M. Mohaghegh, H. Lanjanian and P. H. Abharian, in *Int. Conf. Neural Information Processing* (Springer, Cham, 2020), pp. 796–803.
16. J. Tang, D. Wang, L. Fan, R. Zhuo and X. Zhang, *IEEE Trans. Dielectr. Electr. Insul.* **22**, (2015) 3037.
17. J. M. Li, H. J. Wei, L. D. Wei, D. P. Zhou and Y. Qiu, *Symmetry* **12** (2020) 272 .
18. J. Lin and Q. Chen, *Mech. Syst. Signal Process.* **38** (2013) 515.
19. J. Sun, H. Li and B. Xu, *J. Fail. Anal. Prev.* **16** (2016) 583.
20. Z. Zhang, T. Wen, W. Huang, M. Wang and C. Li, *J. Xray Sci. Technol.* **25** (2017) 261.
21. S. Guan, H. Pang, W. Song and Z. Kang, *Nongye Jixie Xuebao* **34** (2018) 61.
22. G. Cao, Y. Han, Y. Chen and C. Yang, *Mod. Phys. Lett. B* **28** (2014) 1450090.
23. X. Yuan, B. Ji, Y. Yuan, Y. Huang, X. Li and W. Li, *Fractals* **23** (2015) 1550010.
24. G. F. Gu and W. X. Zhou, *Phys. Rev. E* **74** (2006) 061104.

25. F. Wang, Q. Fan and H. E. Stanley, *Phys. Rev. E* **93** (2016) 042213.
26. H. Ma, Z. Cheng, Z. Wang, Y. Gu, T. Zhang, H. Qiu and S. Yang, *Appl. Phys. Lett.* **113** (2018) 083704.
27. M. A. Khan, T. Akram, Y. D. Zhang and M. Sharif, *Pattern Recognit. Lett.* **143** (2021) 58.
28. B. B. Mandelbrot, *J. Fluid Mech.* **62** (1974) 331.
29. C. Meneveau and K. R. Sreenivasan, *Phys. Rev. Lett.* **59** (1987) 1424.
30. E. A. Novikov, *Phys. Fluids* **2** (1990) 814.
31. R. Benzi, L. Biferale, G. Paladin, A. Vulpiani and M. Vergassola, *Phys. Rev. Lett.* **67** (1991) 2299.
32. C. Campbell, *Neurocomputing* **48** (2002) 63.